PCCP

Accepted Manuscript

ROYAL SOCIETY OF CHEMISTRY

www.rsc.org/pccp

Journal Name

RSCPublishing

ARTICLE

Improved Charge Separation via Fe-doping of Copper Tungstate Photoanodes

Cite this: DOI: 10.1039/x0xx00000x

Divya Bohra[a] and Wilson A. Smith*[a],

Received 00th January 2012,
Accepted 00th January 2012

DOI: 10.1039/x0xx00000x

www.rsc.org/

Photoelectrochemical (PEC) water splitting offers a clean pathway to renewable and sustainable energy in the near future. The key to improving the efficiency of PEC devices is the ability to find materials with suitable optoelectronic properties, and identifying, then overcoming their limitations. In this paper, we explore the photoelectrochemical performance of $CuWO_4$ photoanodes for solar water splitting, and find that charge separation is the dominant limitation for this material. As a result, we attempt to dope the material with Fe, the first such example of doping this semiconductor for PEC water splitting. An improvement in performance is achieved for doped films which show 1.5 times the photocurrent density and a 50% higher charge separation efficiency at 1.23 V vs RHE.

Introduction

Addressing the sharply rising demand for energy in a manner that is environmentally benign, sustainable, scalable and equitable is one of the most critical challenges we face today. Solar energy striking the earth's surface is an inexhaustible and sustainable resource which can potentially be harvested to fulfil our rising need for clean and renewable energy. In photosynthesis, energy from sunlight is absorbed by plants and converted into electron hole pairs, of which the holes are utilized to oxidize water to generate O_2 and the electrons are utilized to generate the reduction product NADPH in two separate steps of photosystem I and II. Artificial systems capable of similarly storing the sun's energy in chemical bonds are very desirable to generate renewable fuels and chemicals. Such a technology can circumvent the storage and distribution problems faced by current solar photovoltaics and can provide a stable and constant energy flux through decentralized systems. Photoelectrochemical (PEC) water splitting is a very promising technique that utilizes semiconductor materials to harvest sunlight to generate hydrogen and oxygen, thus providing a simple route to convert solar energy into storable chemical energy.

The O_2 evolution reaction is thermodynamically and kinetically much more challenging compared to the H_2 evolution reaction [1] and requires materials that can withstand oxidizing conditions for a long time without degradation [2]. Development of photoanode materials with suitable properties is one of the most challenging aspects of the PEC water splitting technology. Due to the requirement of stability under oxidizing conditions, most of the photoanode materials investigated have been metal oxides or oxo-metalates [3] starting with the pioneering report on photoelectrochemical water splitting by n-type titanium dioxide (TiO_2) in 1972 [4]. Although significant progress has been made over the past few decades in the development of these materials, further enhancements are needed in terms of efficiency, stability and costs to make this approach economically viable at a commercial scale [5].

Photoanode development has been dominated by large band gap metal oxides such as TiO_2 [4] and WO_3 [6], which are only able to absorb a small portion of the solar spectrum, thus limiting their overall efficiencies and making them non-practical for large scale implementation. Therefore, new materials need to be explored that have smaller band gap energies, and are still comprised of earth abundant materials.

Copper tungstate ($CuWO_4$) is an attractive material as a photoanode for water splitting due to its n-type conductivity, an optical band gap of ~2.3 eV leading to a >10% theoretical Solar-to-Hydrogen (STH) conversion efficiency, stability in aqueous media and it's environmentally benign composition [7], [8].

The use of $CuWO_4$ thin film photoanodes in a redox mediated photoelectrochemical cell was reported for the first time in 2005 by Pandey et al. [9]. A power conversion efficiency of 0.64% was observed for the spray deposited films (0.7 μm thick) using a Ce^{4+}/Ce^{3+} electrolyte and the low efficiency was attributed to high resistance of the cell, low thickness of the film and interface states. As a means to tune the band gap of copper tungsten oxides, amorphous Cu-W oxide films were studied by Chen et al. [10] by varying the Cu:W ratio. The amorphous nature of the films was used to overcome the solubility limit of the crystalline oxide. However, these films had disadvantages such as low charge carrier mobility, high defect density and were unstable in aqueous solutions.

PEC studies on $CuWO_4$ thin films (2-3 μm) prepared by electrodeposition were reported by Yourey and Bartlett [7]. PEC cell measurements with potassium phosphate (KP_i) buffer at pH 7 showed a photocurrent density of 0.16 mA cm^{-2} at +0.5 V (vs. Ag/AgCl) bias potential. It was shown that the addition of methanol to the aqueous electrolyte solution led to a significant increase in the photocurrent, implying an accumulation of holes at the semiconductor/electrolyte interface in the absence of a hole scavenger. The elimination of charge recombination centres was proposed as a measure to improve the efficiency of the process. The same group proposed a Z-scheme using a composite $CuWO_4$-WO_3 thin film for water oxidation with ferricyanide reduction ($[(Fe(CN)_6]^{-3/-4}$) taking place at the platinum-mesh counter electrode in an electrolyte at pH 7 [11]. The system shows low efficiency and quantum yield which is attributed to low charge carrier diffusion length and low absorbed photon flux density. Chang et al. [8] have reported results obtained for $CuWO_4$ films prepared by reactive magnetron co-sputtering. PEC measurements at pH 1.35 in phosphoric acid buffer for the annealed film showed a photocurrent density of 400 μAcm^{-2} at a bias potential of 1.6 V (vs. SCE). A p-n junction formed by the combination of p-type CuO and n-type $CuWO_4$ has been demonstrated by Zheng et al. [12] with $CuWO_4$ deposited on top of the CuO layer at the semiconductor/electrolyte interface due to its favourable band gap position and stability for oxygen evolution half reaction.

Recently, Gaillard et al. [13] reported nanocomposite photoelectrodes of $CuWO_4$ and multi-wall carbon nanotubes (MWCNT) for solar-water splitting where the MWCNT's act as an effective electron collector in the bulk of the electrode. The resultant films showed 30% reduction in bulk resistance to charge transport compared to un-modified $CuWO_4$, and also an enhanced photocurrent density (26% at 0.8 V vs. SCE in pH 10). Also very recently, Yourey and Bartlett have reported the chemical stability of $CuWO_4$ electrodes in KP_i and potassium borate (KB_i) buffers as a function of pH [14]. They demonstrate a high Faradaic efficiency for the films (87%, 79% and 100% at pH 3, 5 and 7 respectively) also in the presence of chloride ions.

It is clear from the previous studies that the bulk charge resistance is a major limitation for $CuWO_4$ photoanodes. Here, we report doping of $CuWO_4$ photoanodes as a potential route to overcome the charge transport and separation limitation of the material. We use a spray pyrolysis technique to deposit nanostructured thin films of $CuWO_4$ using both basic and acidic precursor solutions. The structural, optical, and photoelectrochemical properties of these films were investigated and optimized in order to fabricate highly crystalline films of $CuWO_4$ which have shown promising photoelectrochemical performance.

In addition to fabricating highly active $CuWO_4$ films, we have also successfully doped $CuWO_4$ for the first reported time with iron (Fe). This has shown drastic improvements in the incident photon conversion efficiency (IPCE) and significantly higher photocurrent values in the presence of 5 mM hydrogen peroxide (H_2O_2) in the electrolyte solution. These observations have been explained by an increase in charge carrier density due to the exchange of Cu^{2+} in the lattice with Fe^{3+} resulting in an improved charge carrier mobility. This enhancement in mobility is however accompanied with a detrimental effect on the catalysis at the surface. Although solid solutions of $CuWO_4$ giving $Zn_{1-x}Cu_xWO_4$ [15] and $CuW_{1-x}Mo_xO_4$ [16] have been reported in the past with the aim to tune the band gap, we are not aware of any work exploring the technique of doping as a strategy to overcome the charge transport limitations of copper tungstate photoanodes.

In this study, we have used photoelectrochemical techniques to resolve the obtained photocurrent into contributions from charge carrier generation, separation and catalytic processes thereby giving direct quantitative information about the fundamental material deficiencies for $CuWO_4$. Such identification is imperative in order to understand and engineer better performing photoanodes with higher water splitting efficiency.

Experimental section

Synthesis of $CuWO_4$ Films

$CuWO_4$ films were deposited on conductive FTO-coated glass substrate (fluorine-doped tin dioxide, TEC-15, Hartford Glass Co.) using a spray pyrolysis technique. The substrate temperature was maintained at a constant value during the spray by placing them on a uniformly heated plate. The temperature was measured using a thermocouple pressed to the top of the heat plate. The spray deposition was carried out using a Quickmist air atomizing spray nozzle driven by an overpressure of nitrogen gas. The value of this overpressure was fixed to give a spray rate of 0.16 ml/s. The nozzle-substrate distance was fixed at 21 cm in order to obtain uniform fine droplets at the substrate surface. The precursor solution was placed 20cm below the nozzle and fed to the nozzle via the siphoning effect induced by the nitrogen gas flow. Each spray cycle consisted of

1 s of spray time and 59 s of delay time. After the deposition, the thin films were thermally annealed in a tube furnace at 500°C for 2 h in O_2 atmosphere.

Before deposition, the substrates were cleaned by ultrasonicating for three successive 15 minute sessions in a Triton solution, acetone and isopropanol respectively and dried under a flow of compressed nitrogen gas just before use. The precursor solution was prepared by dissolving copper sulfate pentahydrate ($CuSO_4 \cdot 5H_2O$, 99%, Acros Organics) in double distilled water to which an equimolar amount of sodium tungstate dihydrate ($Na_2WO_4 \cdot 2H_2O$, 99%, Merck KGaA) was added to give a yellowish precipitate of $CuWO_4$. The precipitate was dissolved by adding ammonia (NH_3, 25%, Sigma-Aldrich) to give a resultant basic solution (pH=12.1) with a concentration of 0.1 M of Cu^{2+} and W^{6+} ions. In order to obtain an acidic precursor solution, an appropriate amount of nitric acid (HNO_3, 1 N solution in H_2O, Aldrich) was added to the basic solution until a pH of 1.6 was achieved and a final concentration of 0.01 M of Cu^{2+} and W^{6+} ions was reached by dilution with ultrapure water. For Fe doped samples, the required volume of solution was pipetted from a 0.03 M iron sulfate heptahydrate ($FeSO_4.7H_2O$, 99%, Acros Organics) aqueous solution depending on the dopant concentration desired in the sample. This volume was added to the acidic $CuWO_4$ precursor solution described above. An equimolar amount of tungsten was also added to the solution by pipetting the appropriate volume from a 0.03 M aqueous solution of $Na_2WO_4 \cdot 2H_2O$ (i.e. co-doping of the $CuWO_4$ with Fe and W). The dopant percentage is defined as % (mole of Fe/mole of Cu) in precursor solution.

Material Characterization

The UV-vis absorption of $CuWO_4$ films was measured with a Perkin-Elmer Lamda 900 spectrometer. Spectra were recorded in reflectance (R) and transmittance (T) mode respectively. Tauc plots were generated by plotting $(\alpha h\nu)^n$ versus $h\nu$ where α is the absorption coefficient of the thin film in cm^{-1}, h is the Planck's constant in eV·s, ν is the frequency of the incident light in s^{-1} and n=1/2 owing to the indirect band gap for $CuWO_4$. The band gap energy is given by the value on the x-axis at the point of intersection of tangential lines drawn along the two linear portions of the plot.

The surface morphology and the thickness of the films were studied using Scanning Electron Microscope (SEM) using Jeol JSM-6010LA Analytical SEM machine using an accelerating voltage of 5 kV.

The X-Ray Diffraction (XRD) analysis was performed using a Bruker D8 Advance diffractometer (Co Kα radiation, λ=1.78897 Å) of a conventional X-Ray source powered at 40 kV and 50 mA. The diffraction patterns are obtained by scanning the samples from 20° to 80° (2θ) with a scan speed of 1 sec/step with each step size being 0.02 degrees. The patterns are plotted and compared with data from Joint Committee Powder Diffraction Standards (JCPDS) for analysis. The grain size is calculated using the Scherrer equation and the scattering intensity and angle are used to determine the phase composition of the synthesized films.

Photoelectrochemistry

Photoelectrochemical characterization was carried out in an aqueous 0.1 M potassium phosphate (KP_i) solution buffered to pH 7 with dipotassium phosphate (K_2HPO_4, 99%, J.T. Baker) and monopotassium phosphate (KH_2PO_4, 99.5 %, Fluka). The potential of the $CuWO_4$ working electrode (0.283 cm^2) was controlled by a potentiostat (EG&G PAR 283). A coiled Pt wire and an Ag/AgCl electrode (XR300, saturated KCl and AgCl solution, Radiometer Analytical) were used as the counter and reference electrodes in a three-electrode cell, respectively. The construction of the three-electrode cell has been discussed in detail in chapter 3 of the book edited by van de Krol and Gratzel [17].

White-light photocurrent measurements were performed under simulated AM1.5 solar illumination (100 $mWcm^{-2}$) with a Newport Sol3A Class AAA solar simulator (type 94023A-SR3). Three types of J-V measurements were taken for each sample: under dark, under AM1.5 illumination and under chopped AM1.5 illumination i.e. by turning the illumination of the solar simulator on and off at a fixed frequency. The first two sets of measurements were taken by cycling the voltage between -0.4 V and 1.6 V vs. Ag/AgCl (0.212 V and 2.212 V vs. RHE) for 3 cycles. The potential was swept at a constant rate of 50 mV/s with an initial delay of 5 seconds sweeping 25 mV/step. The third (chopped) measurement was taken between 0 V and 1.6 V vs. Ag/AgCl (0.612 V and 2.212 V vs. RHE) with only 1 cycle from the low potential to the high potential. The rate for the potential sweep for this measurement was kept at 10 mV/s with 5 mV/step.

The incident photon to current conversion efficiency (IPCE) was obtained by monochromatic photocurrents which were measured with a 200 W quartz tungsten-halogen lamp coupled into a grating monochromator (Acton SpectraPro 150i). The bias potential was fixed at 0.618 V vs. Ag/AgCl (1.23 V vs. RHE, the water splitting potential) with a shutter time and aperture of 10 s and 3 s respectively. The start and end wavelength are fixed at 600 nm and 300 nm respectively. The mono-chromatic light intensities were measured with a calibrated photodiode (Ophir PD300-UV) and ranged between 0.3 and 8 $mWcm^{-2}$.

A Frequency Response Analyzer (FRA) module (SI 1255, Schlumberger Technologies Ltd.) coupled with the potentiostat was used to measure the impedance spectra of the thin film electrode. The connections were made as shown in section 3.6.3 of the book edited by van de Krol and Gratzel [17] with a Pt wire as a quasi-reference electrode connected to the reference electrode via a 15 nF capacitor. Measurements were taken at every 0.1 V step between 0 V and 0.5 V vs. Ag/AgCl (i.e. 0.61 V and 1.11 V vs. RHE) as this range of bias potential was between the on-set potential and the potential at which an increase in dark current was observed during steady state J-V measurements on the electrode. A frequency range of 0.01 Hz to 100 kHz was swept with a 10mV amplitude perturbation and

an integration time of 1000 seconds was used with a starting delay of 2 seconds. The measurements were taken under simulated AM1.5 solar illumination described previously. The measurement for the potential of 0.4 V was also performed in the presence of H_2O_2 and in dark. We have chosen 1 mA as the potentiostat's current range giving an internal resistance of 1 kΩ. The buffer solution used in the cell is 0.1 M aqueous KP_i solution at pH 7.

Results

Synthesis and Material Characterization

The deposition of $CuWO_4$ films was broadly divided into three steps; (1) synthesis of the precursor solution (2) spray pyrolysis and (3) the post-deposition treatment of the film. The degrees of freedom associated with each of these steps were identified and varied to systematically optimize the overall deposition process. Here, we discuss the major observations of the optimization process and also suggest routes to further optimize the properties of the films.

Films deposited using a basic precursor solution (pH=12.1) were found to be opaque whereas on the other hand, films with the same thickness deposited using the acidic precursor solution (pH=1.6) were much more transparent to visible light especially post-annealing (Figure S1). The films deposited using the basic solution showed a marked colour change upon annealing (from greenish as-deposited films to lemon yellow annealed films) as compared to the films deposited using the acidic solution which were yellowish at both stages. The reduction in transparency from one solution to another can be due to higher light scattering or the presence of shallow defect states (such as oxygen vacancies) in the film. It should also be noted that the source of Fe ions used for doping the films was only compatible with the acidic solution and would lead to a precipitate in the basic solution. This provided a strong motivation to use the acidic solution instead of the basic for comparing the doped and undoped films.

The temperature of the substrate was set to three different values: 250°C, 350°C and 450°C respectively to see its effect on the optical band gap as well as the structural properties of the films. The films obtained at these temperatures were differentiable visually as shown in Figure S2. The reason for the change in optical properties with deposition temperature needs to be investigated further. A higher temperature (450°C) of the heat plate led to cracking of the glass substrate due to a high temperature gradient across the substrate upon spraying. A lower temperature (250°C) on the other hand resulted in opaque yellow films with dark coloured spots distributed on the surface.

We observed that the thickness of the films was more easily controllable when using a solution with a concentration of 0.01 M as compared to a solution of 0.1 M, since the film thickness deposited per spray cycle was much larger in the latter case. The difference in concentration can, however, affect the structural properties (such as porosity, grain size, etc.) and potentially the optical properties of the films and should be studied in more detail in the future. Such a study for the case of WO_3 has been reported by Kwong et al. [18]. The Tauc plot shown in Figure S3 for film of thickness 1.5-2 μm (300 spray cycles) deposited using the acidic precursor solution (pH=1.6) spray deposited at 350°C followed by annealing reveals a band gap energy of 2.25 eV. The band gap value obtained is very close to those reported in literature for films of similar thicknesses [7], [8], [13]. A higher value of the band gap was observed for films with lower thickness: 2.45 eV for film sprayed using 150 spray cycles as compared to 2.25 eV for thicker film deposited using 300 spray cycles. The increase in the observed optical band gap with decreasing film thickness has also been indicated by Yourey et.al [14]. A shorter path length for absorption has been used to explain this observation. Such a trend of the increase of the band gap with decreasing the film thickness was also observed for WO_3 by Kwong, et al. [18]. They suggest an influence of the relative effects of volume and surface band gaps due to alterations in structure and composition of the two regions. A variation in compressive stresses in the thicker and thinner films is also pointed out as a possible reason. In the case of $CuWO_4$, the CuO_6 octahedron shows Jahn-Teller distortion with lengthening of two opposite CuO bonds [19]. The change in this distortion due to structural variations with film thickness could possibly influence the observed band gap value.

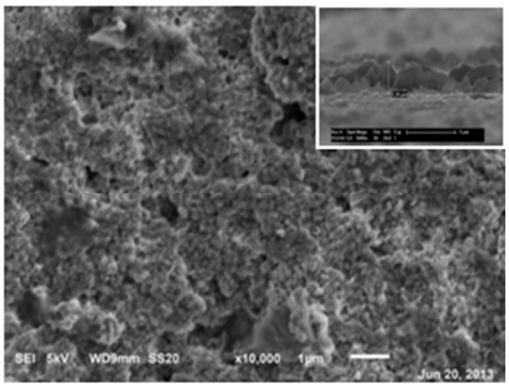

Figure 1. SEM image for film deposited using acidic precursor solution at 350°C substrate temperature followed by annealing at 500°C for 2 h in O_2 taken from top view showing the highly porous surface morphology. Inset top right: SEM image taken at an angle of 1° from the surface close to the film edge showing highly crystalline, sharp and non-uniform features.

Figure S4 compares the light penetration depth against wavelength of incident light for films deposited at 250°C, 350°C and 450°C. It can be concluded that since the films deposited at 250°C are opaque and have minimal transmission, the light penetration depth is very low as compared to films deposited at higher temperatures. The same case is observed for films deposited from the basic precursor solution (pH=12.1) compared to films deposited using acidic precursor solutions (pH=1.6). This is demonstrated in Figure S5. The high

penetration depth for $CuWO_4$ films in general can be attributed to the indirect nature of the band gap and low absorption coefficient for the material.

SEM microscopy indicated noticeable features almost uniformly present across the surface of the films deposited using the acidic solution (Figure 1). The films deposited using the basic solution had a relatively smooth surface. Also, it was found that the film edges were much thicker compared to the centre of the film and showed highly crystalline features (inset of Figure 1). The films deposited using a higher number of spray cycles were found to be more porous than the thinner films. This can be due to a delayed evaporation of the solvent at the surface because of a higher temperature gradient across the thicker film or due to the nature of the film growth mechanism. The thickness of the 300 cycles film varies from 1.5 µm to 2 µm in the cross-section, marking a variation of around 30%. The doping of Fe in these films resulted in no morphological or surface architectural changes.

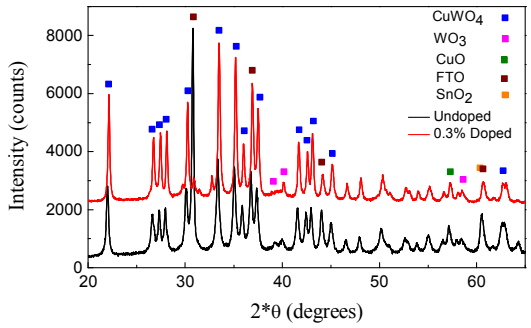

Figure 2. XRD plot with identified peaks for 0.3% Fe doped and undoped $CuWO_4$ films deposited using acidic precursor solution, 350°C substrate temperature and annealed for 2 hours at 500°C in O_2. Both films have a thin layer of SnO_2 deposited on FTO before spray deposition of $CuWO_4$ on the substrate.

The XRD plot for a representative 1.5-2 µm undoped $CuWO_4$ film deposited at 350°C followed by annealing is shown in Figure 2. It can be observed that the film is highly crystalline with several sharp peaks corresponding primarily to the $CuWO_4$ crystal lattice. Three small peaks can also be observed for tungsten oxide (WO_3) and one peak for cupric oxide (CuO). There are several small peaks in the observed XRD pattern around $2\theta=50^o$ (Co Kα X-ray source) that were unidentified in the XRD database.

From the aforementioned results, the conditions used for optimal $CuWO_4$ thin films for further analysis in this report were determined and are as follows: acidic precursor solution (pH=1.6), spray deposition at 350°C, followed by annealing in O_2 at 500°C for 2 h resulting in highly crystalline films with a band gap of 2.25 eV and a film thickness of 1.5-2 µm. In order to improve the charge carrier mobility/diffusion in $CuWO_4$ films, Fe was used as a dopant, since its 3+ oxidation state favourably substitutes for Cu^{2+}. Therefore, for films deposited with Fe, the same deposition parameters were used as the previously mentioned $CuWO_4$ films, and only the precursor solution was changed to incorporate Fe, as described in the experimental section. No Fe phase was visible in the XRD pattern for the 0.3% Fe doped film (Figure 2) which is expected considering the small concentration of Fe added as a dopant to the film. However, after incorporating Fe into the precursor solutions, the XRD peaks for $CuWO_4$ show a slight shift in the diffraction angle (~0.15°), which imply that the crystal lattice of $CuWO_4$ has been given extra strain and/or stress, which is a typical feature found in doped semiconductor films. Therefore, the XRD results suggest that Fe is incorporated into the lattice of the $CuWO_4$ photoanodes.

The XRD pattern in Figure S6 for the as-deposited films with and without Fe dopant shows that the films are less crystalline compared to the annealed films but show mostly similar crystal phases. The sharp rise in intensity after annealing indicates that the as-deposited films are only partially crystalline and the atoms arrange themselves in the preferred crystal planes to a much greater degree upon annealing. It has been reported by Gaillard et al. [13] in the past that a temperature of 450°C is necessary to initiate the crystallization of spray deposited $CuWO_4$ films. However, on the basis of our analysis, diffraction peaks are already visible for as-deposited films for a temperature of 350°C. They identify 500°C as the optimal crystallization temperature for the films which have similar thickness and optical band gap as the films studied in the Figure 2. WO_3 has also been detected by them in the crystal phase up to an annealing temperature of 800°C.

Photoelectrochemistry

Undoped $CuWO_4$ films

PHOTOCURRENT-VOLTAGE MEASUREMENTS The absorption current density (J_{abs}) is defined as the photocurrent that can be obtained if all the photo-generated electron-hole pairs participate in the oxidation of water, as defined in Equation 1:

$$J_{abs} = q\int_{320}^{600} \Phi_\lambda(1 - R - T)d\lambda \qquad \text{Eq. 1}$$

where q is the charge of an electron, Φ_λ is the AM1.5 solar simulator photon flux in $s^{-1}m^2nm^{-1}$ and R and T are the fraction of incident light reflected and transmitted over the wavelength range (determined using UV-vis experiments). This implies that all the photo-generated electron-hole pairs are separated and transported to the surface where the interfacial charge transfer yield is 100% and that the charge carriers only take part in the catalysis of water and not in any other reaction (i.e. we assume 100% Faradaic efficiency). The value of dλ is taken as 2 nm. The value of J_{abs} obtained for the undoped $CuWO_4$ film is 10.43 mA/cm^2. This corresponds to a theoretical solar to hydrogen (STH) conversion efficiency of 12.8% assuming 100% Faradaic efficiency (See Figure S7). Therefore, for a non-ideal $CuWO_4$ photoanode with charge transport or catalytic losses, we can expect photocurrent densities less than 10.43 mA/cm^2, and it is imperative to understand and overcome these deficiencies in the material.

The highest photocurrent obtained for the undoped $CuWO_4$ films with thickness 1.5-2 µm is shown in Figure 3, obtaining a photocurrent density for back illumination of 0.19 mA/cm^2 and 0.1 mA/cm^2 for front illumination at the water splitting potential, 1.23 V vs. RHE. The onset potential for photocurrent is observed to be around 0.94 V vs. RHE for both front and back illumination and the onset of dark current is observed around 2 V vs. RHE. The photocurrent remained stable after several J-V scans. Back illumination gave a much higher photocurrent compared to front illumination indicating at poor electron diffusion in the film [20]. The optimization of film thickness is one of the important factors which can lead to better performing films such that an optimal current can be achieved with the combination of light penetration depth and the diffusion length of the electrons. Our analysis showed that increasing the spray cycle to 300 cycles, and therefore the film thickness to 1.5-2 µm, lead to an increase in both front and back-illumination photocurrent. The trend of number of spray cycles with the measured photocurrent is shown in Figure S8. An increase of surface porosity and a decrease in optical band gap with increasing film thickness could be some of the factors leading to this trend.

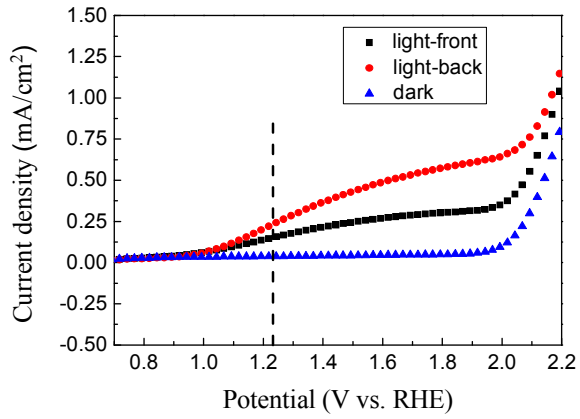

Figure 3. Photocurrent density for 1.5-2 µm thick annealed $CuWO_4$ film for back illumination, front illumination and in dark. The black dashed line signifies 1.23 V vs. RHE i.e. the water splitting potential and the photocurrents (light-dark) obtained at this potential are: back lit: 0.19 mA/cm^2 and front lit: 0.1 mA/cm^2 with dark current: 0.04 mA/cm^2.

A chopped J-V measurement is a very effective way to observe the difference between photocurrent and dark current as well as transients indicating surface recombination processes. The chopped J-V plot for the undoped $CuWO_4$ photoanode under back illumination is shown in Figure 4. It can be seen that the onset potential for the photocurrent is ~0.85 V vs. RHE and the photocurrent obtained at the water splitting potential of 1.23 V vs. RHE is 0.13 mA/cm^2. The figure also shows the photocurrent obtained upon back illumination in the presence of 0.5 M hydrogen peroxide (H_2O_2) in the electrolyte solution for the same sample. H_2O_2 acts as a hole scavenger and ensures no hole accumulation occurs at the semiconductor-electrolyte interface, i.e. we assume there is close to 100% catalytic efficiency using H_2O_2 [21]. As can be seen clearly in Figure 4, H_2O_2 enhances the photocurrent density at the water splitting potential by more than 2 times giving a value of 0.27 mA/cm^2, and the photocurrent onset potential shifts cathodically to ~0.8 V vs. RHE. We can therefore conclude that the catalytic properties of the film have significant room for improvement and that the kinetics of hole transfer from the film surface into the electrolyte is a potential limiting factor to the PEC performance.

Doped $CuWO_4$ films

Some attempts to improve the charge carrier mobility in $CuWO_4$ films have been reported in literature such as the formation of a heterostructure of WO_3 and $CuWO_4$ [11], a p-CuO/n-$CuWO_4$ junction [12], a $BiVO_4$/$CuWO_4$ heterojunction [22] and a nanocomposite photoanode made of $CuWO_4$ and multi-wall carbon nanotubes [13]. Doping with suitable non-isovalent substitutional donor atoms can be a potential strategy to enhance the electron conductivity by increasing the charge carrier density. This technique has not been explored in the current published literature on $CuWO_4$ photoanodes to the best of our knowledge.

A substitutional donor atom can either replace the Cu^{2+} or W^{6+} ion in its respective octahedral site. In order to identify the potential dopant atoms for such a substitution, we primarily consider the factors of oxidation state, ionic size, electronic configuration and the relative abundance and toxicity of the substituting atom. Some of the promising non-isovalent dopant candidates identified by our preliminary study include: Bi^{3+}, Fe^{3+}, Mn^{3+}, Cr^{3+}, Ga^{3+}, In^{3+}, $Ti^{3+/4+}$, Sn^{4+} and Mo^{4+} to substitute Cu^{2+}. Amongst the promising non-isovalent dopant ions mentioned above, Sn^{4+} and Fe^{3+} display the most desirable properties due to their non-toxicity, abundance, closeness to Cu^{2+} in terms of the ionic radius and also the involvement of s orbitals in the case of Sn^{4+}. Hence, for our further investigations, we have used Fe as the dopant atom of choice.

The primary motivation to use non-isovalent substitutional dopant atoms is to increase the carrier concentration in the film and thus enhance the electronic conductivity. Isovalent doping on the other hand can also potentially enhance the conductivity, not by increasing the number of charge carriers, but via other mechanisms that benefit migration of charge carriers in the lattice such as replacement of the localized Cu 3d orbitals with more diffused s orbitals. The promising isovalent dopant candidates identified by our preliminary analysis include first row d-block elements: Mn, Fe, Co, Ni and Zn substituting Cu in the wolframite crystal structure of $CuWO_4$ [23], [24], [25], with Mn^{2+} forming the most promising option considering the criteria of toxicity, abundance, size as well as electronic configuration. Other promising isovalent dopants include Ca^{2+}, Mg^{2+} and Mo^{6+}. Factors such as distortion of the crystal geometry due to incorporation of substitutional dopant ion, contribution of small polaron hopping, potential for the dopant ion to act as an electron trapping site, their interaction with the surrounding O^{2-} ions (such as the strength of the covalent

interaction), formation of crystal defects, have not been taken into account in this analysis and can eventually play a crucial part in the overall performance.

PHOTOCURRENT-VOLTAGE MEASUREMENTS FOR FE DOPED $CuWO_4$ FILMS In this section, we report the results from our attempt to dope $CuWO_4$ films with Fe^{3+} ions with an aim to enhance the conductivity of electrons in the bulk of the photoanode. Fe has been chosen as a dopant because of its abundant non-toxic nature, closeness of the Fe^{3+} as well as Fe^{2+} ionic radii to the Cu^{2+} ion to be substituted and a good compatibility with the wolframite type crystal structure of $CuWO_4$. The reaction Equation 2 represents the incorporation of Fe^{3+} ions in the $CuWO_4$ lattice using Kröger-Vink notation. We add an excess amount of W^{6+} over Cu^{2+} which is equivalent to the Fe^{3+} moles added in order to achieve co-doping by Fe and W.

$$Fe_2O_3 + 2WO_3 \xrightarrow{2CuWO_4} 2W_W^X + 8O_O^X + \frac{1}{2}O_2(g) + 2Fe_{Cu}^{\bullet} + 2e' \qquad \text{Eq. 2}$$

Figure S9 shows the trend in photocurrent density at 1.23 V vs. RHE with and without H_2O_2 for back illumination of the $CuWO_4$ photoanodes as a function of Fe doping concentration. It can be seen that although the photocurrent does not see a significant rise without the presence of a hole scavenger, once H_2O_2 is added to the electrolyte and the catalytic efficiency of the surface is almost a 100%, the photocurrent sees a considerable rise with doping as a result of increase in the number of charge carriers. 0.3 % Fe doped films show the most marked improvement in photocurrent with and without the presence of H_2O_2 and this dopant concentration has therefore been chosen for further analysis in this report. Here we compare the PEC performance of an undoped and a 0.3% Fe doped $CuWO_4$ film both deposited using 300 spray cycles (1.5-2 µm) at 350°C followed by annealing at 500°C for 2 h in O_2.

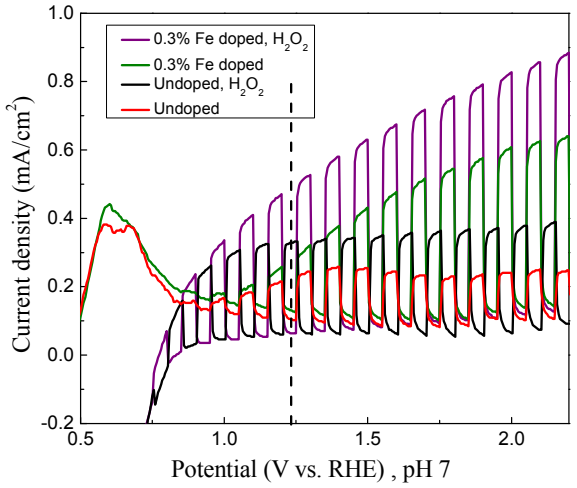

Figure 4. Chopped J-V curve for undoped and 0.3% Fe doped films. The black dashed line represents the water splitting potential: 1.23 V vs. RHE.

Figure 4 shows the chopped J-V for both the undoped and doped films with and without the presence of H_2O_2 in the electrolyte. It can be seen clearly that the presence of the hole scavenger enhances the photocurrent for both films and more so for the Fe doped film. The peak in current density centered around 0.6 V vs. RHE is most likely to the presence of excess W in our films, even though only a negligible amount was detected by XRD. This peak has been previously attributed to the intercalation of H^+ ions into WO_3 during electrochemical cycling [26], [27], [28]. Therefore we attribute this electrochemical peak due to the presence of excess W in our films. At the water splitting potential, the difference between the photocurrents for the doped and the undoped films is not very significant: 0.14 mA/cm^2 and 0.13 mA/cm^2 respectively, but it increases drastically at higher bias voltages. The electrons in the bulk have a higher driving force to reach the semiconductor-electrolyte interface at high bias potentials and hence, the photocurrent observed at higher voltages for doped films, with a greater electron density in the bulk, is much larger compared to the undoped films.

Photocurrent Action Spectra

The incident photon to current conversion efficiency (IPCE) for the two films has been compared in Figure 5 and it can be seen that the IPCE is enhanced for the doped film as compared to the undoped film in the presence of H_2O_2. It can also be seen that the incorporation of Fe into the $CuWO_4$ significantly enhances the IPCE across the spectral range. While the un-doped film has a maximum IPCE of ~1%, the Fe doped film has a maximum around 9%, showing a substantial improvement of converting incident photons into flowing electrons. The enhancement may support the intent of our study, which was to increase the charge carrier density of the films with non-isovalent doping, which results in a larger extracted current density. We also suspect that the lower light intensity used for measurement of the IPCE spectra detrimentally affects the absorption, separation and recombination processes in the possibly defect-rich undoped films, further lowering the IPCE compared to Fe doped films.

Estimation of Catalytic and Separation Efficiency

To engineer better performing photoanodes, it is essential to explicitly determine the rate-limiting factors. The following analysis was used by Dotan et al. [21] to identify performance limitations for hematite. The observed photocurrent in an aqueous electrolyte can be defined as in Equation 3:

$$J_{H2O}=J_{abs}*\eta_{sep}*\eta_{cat} \qquad \text{Eq. 3}$$

where J_{H2O} is the photocurrent density observed for water splitting, η_{sep} is the efficiency with which the photo-generated charges are separated or the efficiency of transport of the generated charges to the semiconductor-electrolyte interface and η_{cat} is the efficiency of interfacial/catalytic charge transfer.

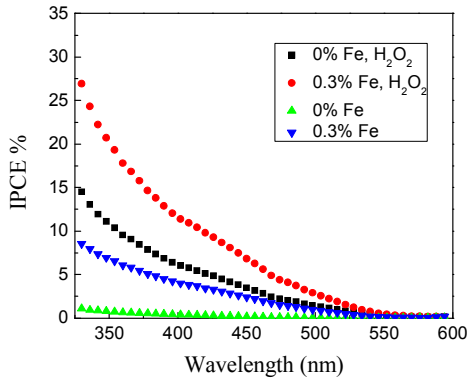

Figure 5. IPCE as a function of wavelength of incident light for undoped and 0.3% Fe doped films

Similarly, the photocurrent measured in H_2O_2, J_{H2O2}, can be defined as Equation 4:

$$J_{H2O2}=J_{abs}*\eta_{sep} \quad \text{Eq. 4}$$

owing to the fact that the catalytic efficiency can be estimated to be 100% in the presence of H_2O_2, which acts as a hole scavenger. Dividing Equation 3 by Equation 4 gives the expression:

$$J_{H2O}/J_{H2O2}=\eta_{cat} \quad \text{Eq. 5}$$

From the η_{cat} vs. bias potential plot (black hollow data points) shown in Figure 6, we can estimate that 40% of the photogenerated holes that reach the semiconductor-electrolyte interface at a bias potential of 1.23 V vs. RHE are not injected into the electrolyte and hence do not participate in water oxidation. The catalytic efficiency rises from almost close to 0 near the onset potential for the films to around 70% at higher anodic potentials. This increase is expected as the surface traps are filled at higher applied potentials and less accumulation of holes occurs at the semiconductor-electrolyte interface. Therefore, routes to enhance the catalytic properties of the film surface such as the addition of oxygen evolution catalysts (OECs) can considerably enhance the performance of $CuWO_4$ photoanodes. In addition to the catalytic properties of these films, the charge separation efficiency can be estimated by Equation 6 shown below:

$$J_{H2O2}/J_{abs}=\eta_{sep} \quad \text{Eq. 6}$$

From the plot of η_{sep} vs. bias potential in Figure 6 (red hollow data points), it can be seen that the separation efficiency at the water splitting potential is only 3% for the undoped sample and greater than 4% for the Fe doped sample. Furthermore, at higher potentials, the improvement in charge separation efficiency is much more dramatic, with the charge separation efficiency nearly double at 2 V vs. RHE. These trends clearly show that the incorporation of Fe into $CuWO_4$ has the ability to significantly enhance the charge separation efficiency, though the overall efficiency (~8%) is still quite low. This is clearly the most critical aspect which needs to be improved in order to enhance the overall performance of $CuWO_4$ photoanodes.

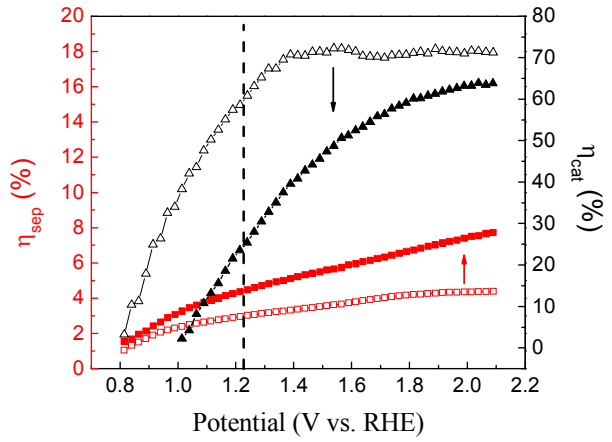

Figure 6. Separation efficiency (in red) and catalytic efficiency (in black) for undoped films (hollow data points) and 0.3% Fe doped films (solid data points) vs. the applied bias voltage. The black arrow downwards shows the decreasing catalytic efficiency on doping with η_{cat}=60% and 24.5% for the undoped and doped film respectively at 1.23 V vs. RHE. The red arrow going upwards shows the increasing separation efficiency on doping with η_{sep}=3% and 4.5% for the undoped and doped film respectively at 1.23 V vs. RHE

It was found that the catalytic efficiency reduced considerably upon doping the film whereas the separation efficiency was enhanced at the water splitting potential as can be seen in Figure 6. The increase in separation efficiency validates our approach to use Fe doping as a means to enhance the bulk electron conductivity. The difference between the surface catalysis for doped and undoped films might be because of incorporation of surface defects due to the presence of Fe.

Electrochemical Impedance Spectroscopy (EIS)

The data obtained for the impedance spectroscopy scan for bias potentials ranging from 0 V to 0.5 V vs. Ag/AgCl is shown in the form of a Nyquist plot in Figure S10. In the plots for each of the bias values, two slightly depressed semicircles can be seen overlapping each other. Similar Nyquist plots for annealed $CuWO_4$ films have been reported by Chang et al. [8]. Figure S11 shows the trend of the values obtained for circuit elements of the equivalent circuit (Figure 7.a) on fitting the impedance data. The equivalent circuit distinguishes between the space charge region (Rsc and CPEsc) and the surface states (Rss and CPEss). In this model the charge transfer can only occur through the valence band edge on the semiconductor electrolyte interface. It was observed that the time constant for the process at the surface states was much lower than the one at the space charge region at lower applied bias voltage, and the difference reduced as the voltage was increased. The parameter values and the corresponding error values obtained on model fitting can be found in the supplementary information in Table S1. Rsol includes resistances such as the electrolyte, the back contact, wires and is therefore expected to remain constant with voltage.

The fitted value of Rsol showed a variation of around 9% across the potential range. The trend of the space charge resistance (Rsc) shows an almost exponential decay in the resistance across the space charge region with bias potential. It should also be noted that the magnitude of the space charge resistance is very high and confirms our earlier observation of electron transport being a limitation. The surface state resistance (Rss) is the resistance to the movement of the charge carriers from the valence band or the conduction band into the surface state traps. The Rss shows a trend opposite to that shown by the space charge resistance. It rises almost exponentially with an increase in bias voltage and then dips again after 1 V vs. RHE (0.4 V vs. Ag/AgCl). As the bias voltage is increased, the space charge width rises and the charge carriers find it easier to move through the space charge region to the valence band edge due to the strong electric field in the region. The trend in the surface state capacitance (Css) is a linear decrease with increasing bias voltage implying a lesser accumulation of charges in the surface state traps with increasing bias voltage.

The Nyquist plots for the impedance spectra at 0.4 V bias potential vs. Ag/AgCl were measured for the three cases; 1) under AM 1.5 illumination, 2) in the presence of H_2O_2 under AM 1.5 illumination and 3) in dark, and are shown in Figure 7.b. The space charge width decreases upon illumination of the semiconductor-electrolyte interface due to excitation of charge carriers from the valence band to the conduction band. The decreasing of Rsc (lower frequency semi-circle becomes smaller) on illumination can be due to an increase in conductivity due to higher number of charge carriers in the bands. The space charge resistance is observed to decrease even more drastically on the addition of H_2O_2 to the electrolyte. This can be due to the fact that the addition of the hole scavenger prevents any accumulation of holes near the valence band edge leading to a greater driving force (or reduced catalytic potential needed) for the holes to travel across the space charge width to the band edge. The trend of Rss (seen from radius of the higher frequency semi-circle) value is similar to the one seen earlier in Figure S11.a with the value of the resistance decreasing on decreasing space charge width (upon illumination). The addition of H_2O_2 does not lead to any significant change in the value of Rss compared to the one without H_2O_2.

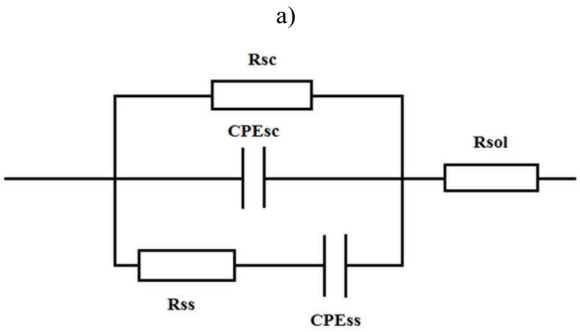

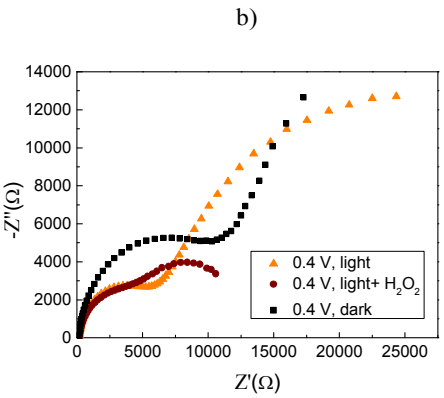

Figure 7. a) Equivalent Circuit (EC) with the space charge resistance (Rsc), space charge capacitance (CPEsc), the resistance to the flow of charges to the surface states (Rss), the surface state capacitance (CPEss) and resistance to charge transport by the electrolyte solution in addition with resistance of the conductive back contact, wires, etc. (Rsol).b) Nyquist plots comparing the impedance spectra for a bias voltage of 0.4 V vs. Ag/AgCl for the three cases of 1) under 1 sun illumination, 2) in the presence of H_2O_2 under 1 sun illumination and 3) in dark.

Conclusions

Highly porous, crystalline and nanostructured $CuWO_4$ photoanode films have been deposited using a spray pyrolysis technique. The spray deposition parameters have been optimized so as to give films with the most desirable optoelectronic and crystal properties and the least practical limitations. The J-V measurements for 1.5-2 μm thick film have shown a photocurrent onset potential of ~0.85 V vs. RHE and a photocurrent of 0.13 mA/cm^2 at 1.23 V vs. RHE for back illumination. Charge separation efficiency has been identified to be the major limiting factor for performance and promising dopants have been identified for incorporation in $CuWO_4$ with an aim to enhance the electron conductivity. The PEC performance of the film co-doped with Fe and W has been studied and it was found that doping enhanced the separation efficiency by 50%. Fe doping of $CuWO_4$ photoanodes in conjunction with dedicated OEC's on the surface to enhance catalytic efficiency may offer a route to high efficiency solar water splitting photoanodes.

Acknowledgements

This research is sponsored by a NWO VENI grant (WAS).

Notes and references

[a] Delft University of Technology, Materials for Energy Conversion and Storage, Department of Chemical Engineering, 2628 BL Delft, The Netherlands. Email: W.Smith@tudelft.nl.

† Electronic Supplementary Information (ESI) available: [details of any supplementary information available should be included here]. See DOI: 10.1039/b000000x/

References

[1] T. A. Betley, Q. Wu, T. Van Voorhis and D. G. Nocera, "Electronic Design Criteria for O—O Bond Formation via Metal Oxo Complexes (Special Oxygen Forum Issue)," Inorg. Chem., vol. 47, pp. 1849-1861, 2008.

[2] M. Kanan and D. Nocera, "In Situ Formation of an Oxygen-Evolving Catalyst in Neutral Water Containing Phosphate and Co^{2+}," Science, vol. 321, pp. 1072-1075, 2008.

[3] M. G. Walter, E. L. Warren, J. R. McKone, S. W. Boettcher, Q. Mi, E. A. Santori and N. S. Lewis, "Solar Water Splitting Cells," Chem. Rev., vol. 110, p. 6446–6473, 2010.

[4] K. Honda and A. Fujishima, "Electrochemical Photolysis of Water at a Semiconductor Electrode," Nature, vol. 238, pp. 37-38, 1972.

[5] J. R. Durrant and A. J. Cowan, "Long-lived charge separated states in nanostructured semiconductor photoelectrodes for the production of solar fuels," Chem. Soc. Rev., vol. 42, pp. 2281-2293, 2012.

[6] H. H. Kung, H. S. Jarrett, A. W. Sleight and A. Ferretti, "Semiconducting oxide anodes in photoassisted electrolysis of water," J. Appl. Phys., vol. 48, 1977.

[7] J. E. Yourey and B. M. Barlett, "Electrochemical deposition and photoelectrochemistry of $CuWO_4$, a promising photoanode for water oxidation," J. Mater. Chem., vol. 21, p. 7651–7660, 2011.

[8] Y. Chang, A. Braun, A. Deangelis, J. Kaneshiro and N. Gaillard, "Effect of Thermal Treatment on the Crystallographic, Surface Energetics, and Photoelectrochemical Properties of Reactively Cosputtered Copper Tungstate for Water Splitting," J. Phys. Chem. C, vol. 115, p. 25490–25495, 2011.

[9] P. K. Pandey, N. Bhave and R. Kharat, "Spray deposition process of polycrystalline thin films of $CuWO_4$ and study on its photovoltaic electrochemical properties," Materials Letters, vol. 59, 2005.

[10] L. Chen, S. Shet, H. Tang, K.-s. Ahn, H. Wang, Y. Yan, J. Turner and M. Al-Jassim, "Amorphous copper tungsten oxide with tunable band gaps," J. Appl. Phys., vol. 108, 2010.

[11] J. E. Yourey, J. B. Kurtz and B. M. Bartlett, "Water Oxidation on a $CuWO_4$–WO_3 Composite Electrode in the Presence of $[Fe(CN)_6]_3$–: Toward Solar Z-Scheme Water Splitting at Zero Bias," J. Phys. Chem. C, vol. 116, p. 3200–3205, 2012.

[12] J. Y. Zheng, G. Song, C. W. Kim and Y. S. Kang, "Facile preparation of p-CuO and p-CuO/n-$CuWO_4$ junction thin films and their photoelectrochemical properties," Electrochimica Acta, vol. 69, p. 340– 344, 2012.

[13] N. Gaillard, Y. Chang, A. DeAngelis, S. Higgins and A. Braun, "A nanocomposite photoelectrode made of 2.2 eV band gap copper tungstate ($CuWO_4$) and multi-wall carbon nanotubes for solar-assisted water splitting," International journal of hydrogen energy, 2013.

[14] J. E. Yourey, K. J. Pyper, J. B. Kurtz and B. M. Bartlett, "Chemical Stability of $CuWO_4$ for Photoelectrochemical Water Oxidation," J. Phys. Chem. C, vol. 117, no. 17, p. 8708–8718, 2013.

[15] J. E. Yourey, J. B. Kurtz and B. M. Bartlett, "Structure, Optical Properties, and Magnetism of the Full $Zn_{1-x}Cu_xWO_4$ ($0 \le x \le 1$) Composition Range," Inorg. Chem. , vol. 51, pp. 10394-10401, 2012.

[16] J. C. Hill, Y. Ping, G. A. Galli and K.-S. Choi, "Synthesis, photoelectrochemical properties, and first principles study of n-type $CuW_{1-x}Mo_xO_4$

electrodes showing enhanced visible light absorption," Energy Environ. Sci. , vol. 6, pp. 2440-2446, 2013.

[17] R. v. d. Krol and M. Gratzel, Photoelectrochemical Hydrogen Production, Springer, 2011.

[18] W. Kwong, N. Savvides and C. Sorrell, "Electrodeposited nanostructured WO_3 thin films for photoelectrochemical applications," Electrochimica Acta, vol. 75, pp. 371-380, 2012.

[19] L. Kihlborg and E. Gebert, "$CuWO_4$, a Distorted Wolframite-Type Structure," Acta Cryst., vol. B26, 1970.

[20] Y. Liang, T. Tsubota, L. P. A. Mooij and R. v. d. Krol, "Highly Improved Quantum Efficiencies for Thin Film $BiVO_4$ Photoanodes," J. Phys. Chem. C, vol. 115, pp. 17594-17598, 2011.

[21] H. Dotan, M. Sivula, A. Rothschild and S. C. Warren, "Probing the photoelectrochemical properties of hematite (a-Fe_2O_3) electrodes using hydrogen peroxide as a hole scavenger," Energy Environ. Sci. , vol. 4, pp. 958-964, 2011.

[22] S. K. Pilli, T. G. Deutsch, T. E. Furtak, L. D. Brown, J. A. Turner and A. M. Herring, "$BiVO_4$/$CuWO_4$ heterojunction photoanodes for efficient solar driven water oxidation," Phys. Chem. Chem. Phys., vol. 15, 2013.

[23] O. Khyzhun, V. Bekenev and S. Yu.M., "First-principles calculations and X-ray spectroscopy studies of the electronic structure of $CuWO_4$," Journal of Alloys and Compounds, vol. 480, p. 184–189, 2009.

[24] M. Lalic, Z. Popovic and F. Vukajlovic, "Electronic structure and optical properties of $CuWO_4$: An ab initio study," Computational Materials Science, vol. 63, pp. 163-167, 2012.

[25] R. D. Shannon, Acta Crystallographica, vol. A32, 1976, pp. 751-767.

[26] S.-H. Baeck, K.-S. Choi, T.F. Jaramillo, G.D. Stucky and E.W. McFarland, "Enhancement of photocatalytic and electrochromic properties of electrochemically fabricated mesoporous WO3 thin films", *Advanced Materials*, 2003, **15**, 1269

[27] W. Cheng, E. Baudrin, B. Dunn and J.I. Zink, "Synthesis and electrochromic properties of mesoporous tungsten oxide", *Journal of Materials Chemistry*, 2001, **11**, 92.

[28] W. Smith, A. Wolcott, R. C. Fitzmorris, J.Z. Zhang and Y.P. Zhao, "Quasi-core-shell TiO2/WO3 and WO3/TiO2 nanorod arrays fabricated by glancing angle deposition for solar water splitting", *Journal of Materials Chemistry*, 2011, **21**, 10792.